

# Correlating the radio emission profile and spin-down rate of pulsars using principal component analysis

Livvy Hancock\*, experiment performed in collaboration with Alice Gane under the supervision of Benjamin Shaw, Patrick Weltevrede, Danai Antonopoulou<sup>1</sup>

*Department of Physics, University of Manchester, Greater Manchester, M13 9PL*

(\*Electronic mail: olivia.hancock@student.manchester.ac.uk)

(Dated: 24 May 2024)

Pulsar spin-down rate ( $\dot{\nu}$ ) has been linked to its emission state; we present present principal component analysis (PCA) as a method for characterising the emission state and quantifying its evolution over time. PCA successfully extracted the two emission states of PSR B1828-11 and found that changes in emission profile were correlated to  $\dot{\nu}$  with a correlation coefficient of  $0.66 \pm 0.06$ , which is concurrent with current literature<sup>1, 2</sup>. Our findings suggest that radio emissions from PSR B1822-09 are more complex than a two state system. Whilst PSR B1822-09 shows oscillation between two states in one mode, it also exhibits other changes in its emission profile that occur on different timescales. It demonstrates very low correlation of  $0.13 \pm 0.04$  for pre-2009 data and  $-0.05 \pm 0.04$  for post-2009 data between the most significant mode switching (Q and B modes) and  $\dot{\nu}$ . We suggest this is because changes in  $\dot{\nu}$  are caused by the combined effect of all the changes in emission which is not captured by just this one mode.

## I. INTRODUCTION

Pulsars were discovered in 1967 as periodic variations in radio emissions reaching earth. Signals of 0.3 s duration and a 1.337 s repetition period were detected<sup>3</sup>. Whilst periodic signals such as these had been detected previously, they were not recognised, as pulsed signals were generally regarded as interference and were not something astrophysicists were looking for. Initially, it was unclear whether the signal was terrestrial but the lack of parallax error suggested celestial origin. Furthermore, the signals occurred 4 minutes earlier each day, as is characteristic of a celestial signal, so it was concluded that something new had been discovered. This was not released to the press to avoid alien hysteria<sup>4</sup>; instead in 1968 a paper was published by Hewish announcing the findings and ‘tentatively’ suggesting white dwarf or neutron stars as possible origins for the behaviour. The ‘new’ type of star was termed a pulsar that year and Hewish received a Nobel prize for the discovery though it was actually Bell, a student of his, that made the pioneering recordings of the pulsar.

It is now confirmed that a pulsar is a rotating neutron star that emits beams of electromagnetic radiation. The highly magnetic region around the pulsar is known as its magnetosphere, the geometry of the magnetosphere and its interaction with charged particles is what causes the electromagnetic radiation, though a full model of the emission mechanisms is yet to be established. The rotation axis may be different from the axis of emission. Neutron stars are the final stage in the life-cycle of stars with mass originally in the range of around 8 to 20 solar masses,  $M_{\odot}$ <sup>5</sup>. The gravitational force of a massive star exploding into a supernova compresses the neutrons into a star with density of around  $6.7 \times 10^{14} \text{ g cm}^{-3}$ <sup>5</sup>. This density is calculated assuming a mass of  $1.4 M_{\odot}$  and a radius,  $R$  of  $10 \text{ km}$ <sup>5</sup> which are standard for a neutron star<sup>5</sup>.

Each pulsar is characterised by a distinct emission profile that can exhibit changes on a timescale of hours to days<sup>6</sup>. These changes are called mode switches and will often be between two distinct emission modes (or states). The different emission states of a pulsar can be classified using a metric called the shape parameter (SP). A relation has been found between the emission mode and  $\dot{\nu}$  of a pulsar<sup>7</sup>. We will be using PCA to extract the SP and compare it to  $\dot{\nu}$  to identify whether they are correlated. This could be applied to pulsar timing models, which are models predicting the times of arrival (TOAs) of the pulses to earth.  $\dot{\nu}$  could be added to the model from knowledge of the emission state as this can be more accurately observed than  $\dot{\nu}$ . A more accurate timing model would allow more precise prediction of TOAs, not only advancing understanding of the mechanisms governing pulsar rotation but extending to areas of physics. Pulsar timing observations lead to the discovery of the first exoplanet in 1992<sup>8</sup> and are currently being used to test predictions made by theories of general relativity<sup>9, 10</sup>.

## II. THEORY

### A. Timing noise and Spin-down rate

A timing model is a framework that predicts the arrival time of pulses by optimising a number of parameters based on observations such as rotation period, its position in the sky and whether it is in a binary system. The measured TOAs are adjusted such that they represent the TOA in the inertial reference frame of the the pulsar<sup>11</sup>.

Whilst the arrival times of pulses to earth are characteristically regular, there is error in the predicted and observed arrival times known as timing noise (or residuals). A model can be fit to the residuals which shows the pulsars spin-down behaviour. The presence of the residuals demonstrates error in the timing model and the shape of the residuals can be

used to identify potential sources. Linear residuals suggest an error in the pulse period given to the model whereas quadratic variation suggests error in  $\dot{\nu}^{12}$ .

The timing residuals of the pulsars presented in BHK are dominated by quasi periodic structures, varying on different timescales. The cause of periodic spin-down variability is still contested: one hypothesis is that free precession of the spin axis biases the state of the magnetospheric emission causing changes in  $\dot{\nu}$  rate<sup>13</sup>. The abruptness of the changes to  $\dot{\nu}$  could weaken the case for free precession, an orbiting quark planet has been suggested as an alternative explanation for the periodic changes in  $\dot{\nu}^{14}$ .

### B. Structure of the neutron star

A pulsar consists of distinct regions with different properties defined by the densities at different radii from the core of the star. This is caused by the increase in density towards the core. The outer crust region, seen on figure 1, is crystal lattice made mainly of iron atoms so the neutrons in this region are generally found in the nuclei of the atoms. This is not the case moving radially inwards, as at a density of  $4 \times 10^{11} \text{ g cm}^{-3}$ , the gravitational pressure becomes too large for neutrons to stay bound in their atoms and they ‘drip’ out. The density at which this change of structure occurs is termed the neutron drip point which defines the transition to the inner crust. The inner crust still consists of a lattice of nuclei but there is also an electron gas and a superfluid neutron gas. At the density of nuclear matter,  $\rho_n$ , of  $2.7 \times 10^{14} \text{ g cm}^{-3}$ , the crust dissolves and the liquid interior region begins. This is a superfluid consisting 95% of neutrons and 5% of protons and electrons<sup>5</sup>. The protons also form a superfluid but the highly relativistic electrons do not: they have little effect on the angular momentum and therefore rotation of the star. The structure of the centre of the star is the topic of ongoing research. Whether the core reaches a density where it becomes distinct from the neutron fluid is not confirmed. There has been suggestion that the core could be governed by the strong force and consist of quarks and gluons if the pressure is sufficient to dissolve neutrons to their quark constituents. Pion condensation has also been proposed to comprise the core<sup>15</sup>.

### C. Superfluidity and glitches

At a density above  $\rho_n$ , the neutrons are so densely packed that they occupy quantum states with the same energy: the system is highly degenerate. The mechanics of the system are thus governed quantum mechanically rather than classically. Neutrons are fermions and thus may not occupy the same quantum state as dictated by the Pauli exclusion principle so due to the high densities, neutrons pair into bosons which at low temperatures, like those found in neutron stars, may become Bose-Einstein condensate. The pairing occurs via the attractive part of the strong force. Bose-Einstein condensates exhibit superfluid behaviour so neutron superfluid

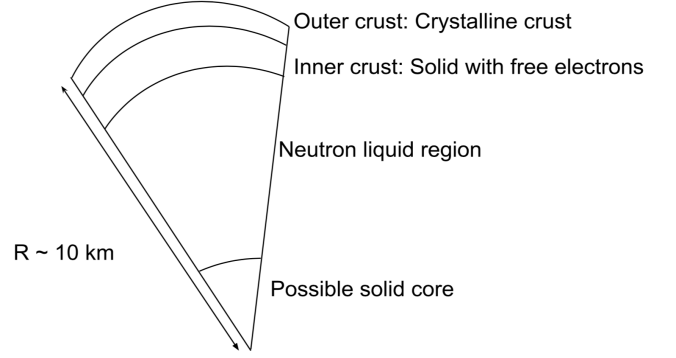


FIG. 1. A schematic showing a slice of the neutron star highlighting the different layers within the star.

will flow freely without energy dissipation to container walls or within the fluid. It has no viscosity and, when there is rotation, exhibits quantised vortices. It is thought that the protons also become superfluid and hence superconducting as they are charged. Electrons do not as electron phonon coupling is too weak<sup>16</sup>. Change in angular momentum must be due to creation or cessation of vortices in the liquid neutron region. The vortices in the neutron liquid region carry angular momentum and therefore affect the total angular momentum of the pulsar and the  $\dot{\nu}^{17}$ . The neutron superfluid in the inner crust rotates at a different rate to rest of the star which is thought to be the causes of glitches<sup>16</sup>. Glitches result in a short term increase in  $\dot{\nu}^{18}$ , but they manifest as a peak in  $\dot{\nu}$  time series. This makes it hard to identify whether a peak in  $\dot{\nu}$  is a glitch or a regular spin-down event. Glitches have also been linked to changes in emission mode<sup>1</sup>.

### D. The magnetic field

Estimates for the magnetic field in a pulsar can be found by considering conservation of magnetic flux,  $\Phi_B$ , the magnetic field,  $B_1$ , and radius  $R_1$  of the progenitor of pulsar. When the progenitor explodes into a supernovae compressing the neutrons into a neutron star, it must have the same flux density as the progenitor.  $\Phi_B = \int_S \mathbf{B} \cdot d\mathbf{S}$  so by equating the flux of the progenitor and neutron star it can be found that the magnetic field of the pulsar,  $B_2$ , is

$$B_2 = B_1 \frac{R_1^2}{R}. \quad (1)$$

Using estimates of  $B_1 \sim 10^3 \text{ Gauss}^{19}$ ,  $R_1 \sim R_\odot$  and  $R \sim 10 \text{ km}$ ,  $B_2$  can be found to be of order  $10^{12}$ . This is a reasonable estimate as the polar field strength of a pulsar is of order  $10^{10}$  to  $10^{12} \text{ Gauss}$  and can reach up to  $10^{14} \text{ Gauss}$  for magnetars which are highly energetic X-ray emitting stars.  $10^{14} \text{ Gauss}$  is the highest field currently known in the universe. Whilst the magnetic field does not have a large influence on the structure

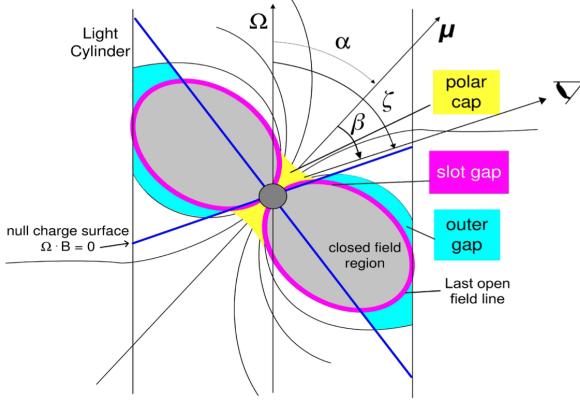


FIG. 2. A representation of the pulsar magnetosphere and light cylinder enclosing it taken from Breed et al. (2015)<sup>20</sup>. The spin axis is vertical and the emission axis is at an angle  $\alpha$  to it, shown in red.  $\omega$  labels the spin-down angular frequency. The polar cap is labelled in yellow and the outer gap in blue.

of the pulsar, it does heavily influence the internal dynamics of the pulsar as the protons and electrons experience the strong field. The effects of the magnetic field differ in the solid crust with free electron region and the neutron superfluid region<sup>16</sup>.

### E. Emission and the magnetosphere

The complete mechanism for pulsar emissions remains elusive: a model that fully explains all the phenomena associated with pulsar emission has not yet been established<sup>21</sup>. A model was proposed in 1969 by Goldreich et al.<sup>22</sup> describing the magnetosphere and how particles interact with it for an aligned rotator (a rotator in which the emission and rotation axis are the same). As the radial distance from the star increases, the velocity at which a particle would have to travel at to co-rotate with the star also increases. This concept defines the light cylinder which is in figure 2 as the distance at which a particle would no longer be able to co-rotate with the star. Charged particles will flow along the field lines in the magnetosphere, co-rotating with the pulsar. However field lines extending outside the light cylinder will cause a flow of particles out of the magnetosphere. Goldreich suggested that the efflux of particles from the magnetosphere carried energy out of the pulsar which resulted in rotational energy loss, increasing the period. The origins of the radio emission and their properties are still not adequately explained by this model. Ruderman and Sutherland<sup>23</sup> in 1975 proposed that the efflux of negative charge is not balanced by reactions at the stellar surface causing a depleted charge region between the surface and the open field lines known as the polar cap, see the yellow region of figure 2. The high potential difference creates an environment conducive to pair production. The positrons produced are accelerated by the electromagnetic fields producing a ‘primary

plasma’ and emit curvature radiation causing producing a ‘secondary plasma’ from which coherent microwaves are emitted. This model explains various features observed such as the micro-structure of pulses and begins to provide an explanation of the emission mechanisms. The radio emissions originate from this secondary plasma however it is now thought they can also be emitted from another region further out in the magnetosphere called the outer gap by similar mechanisms<sup>24</sup>. The outer gap is illustrated on figure 2.

When the emission reaches earth, telescopes can only observe a cut through the beam of emission so decoding our observations of the pulses requires an understanding of the shape of the beam being emitted. Rankin proposed a model where the beam contains patches of radiation, explaining why many pulse profiles exhibits components, not just a simple pulse<sup>25</sup>. An example of a pulse with components is the Q mode shown on figure 3: there is a leading component (higher peak) and a slightly trailing component (slightly lower peak) making up the first pulse on the figure. It is therefore that possible when observing mode switching, one is seeing a different cut through the same shaped emission beam due to the angle of the pulsar emission changing relative to earth. It is not currently known whether mode switching is an observation of the change of viewing angle of emission or a change of the emission profile.

For a pulsar with an emission axis at an angle  $\alpha$  from the rotation axis and a magnetic field  $B_p$  at the pole (independent of the internal field), the rate of energy loss due to electromagnetic emission can be written:

$$\dot{E} = -\frac{B_p^2 R^6 v^4 \sin^2 \alpha}{6c^3}. \quad (2)$$

$v$  is the angular velocity of rotation and  $c$  is the speed of light. This is the oblique rotator model so in a vacuum. This equation links rate of energy loss to the angular velocity of rotation. Rotational energy can be written in terms of the moment of inertia of the pulsar,  $I$ , as

$$E = \frac{1}{2} I \omega^2, \quad (3)$$

which means the rate of change of rotational energy is

$$\dot{E} = I \omega \dot{\omega}. \quad (4)$$

$\dot{\omega}$  is the rate of change of the angular momentum which is proportional to  $\dot{E}$  which is negative.  $\omega = 2\pi\nu$  so  $\dot{\nu}$  is also negative hence the name spin-down rate.

Nulling is a phenomena where the pulsar ‘turns off’, meaning emission is reduced by at least a factor of ten over one or more pulse periods and then increases again<sup>26</sup>. Like mode switching, nulling is thought to be the result of magnetospheric changes<sup>27</sup>. In 2006, Kramer et al.<sup>7</sup> showed that there

TABLE I. A summary of the properties of the two pulsars studied. The epoch refers to the epoch at which the  $\nu$  and  $\dot{\nu}$  were measured at, as evidently they are changing variables.  $\tau_{char}$  is the approximate characteristic age of the pulsar. The data quoted in this table is from Shaw et al. (2022)

PSR	Epoch(MJD)	$\nu$ (Hz)	$\dot{\nu}$ ( $10^{-15}\text{Hzs}^{-1}$ )	$\tau_{char}(\text{kyr})$
B1822-09	52740	1.30	88.57	200
B1828-11	53311	2.47	365.49	100

is a faster  $\dot{\nu}$  when the pulsar is ‘on’. This was explained by increased breaking torque,  $T$ , exerted on the pulsar by the emissions which is given by:

$$T \sim \frac{2}{3c} I_{pc} B_0 R_{pc}^2, \quad (5)$$

where  $B_0$  is the field at the stellar surface,  $I_{pc}$  is the current along field lines at the polar gap and  $R_{pc}$  is radius to the field line crossing the polar cap. The rotational energy loss due to the emissions is  $\dot{E} = T\omega$ . The total energy loss when a pulsar is ‘on’ is thus:

$$\dot{E}_{tot} = I\omega\dot{\omega} + T\omega. \quad (6)$$

It can thus be seen that the rate of change of rotational energy of the pulsar which affects  $\dot{\nu}$  is increased when a breaking torque from the emissions is present.

## F. Radio Emission profiles

PSR B1822-09 and B1828-11 were selected as they have been previously shown to have clearly defined emission modes and drastically different  $\dot{\nu}$  states (LHK), (SSW). The  $\dot{\nu}$  time series for PSR B1828-11 presents a regularly oscillating  $\dot{\nu}$  with a period of around 200 days whereas the  $\dot{\nu}$  PSR B1822-09 is more erratic with small amplitude oscillations followed by large spikes that don’t seem periodic. By studying both pulsars we can thus test whether our method is robust across sources with different behaviours. The spin frequency ( $\nu$ ) and  $\dot{\nu}$  are summarised in table I.

### 1. PSR B1822-09

The different pulses in the mean profile shown in figure 3 represent the signal intensity received at different phases of one rotation. The first is the precursor (PRC), at around the 200th phase bin. The second and most intense pulse is the main pulse (MP) at around bin 250 and the third and least bright is the interpulse (IP) at around bin 800. The IP is seen at 180 degrees of rotation and suggests that the rotation axis is almost perpendicular to the emission axis which is parallel to the line of site to earth.

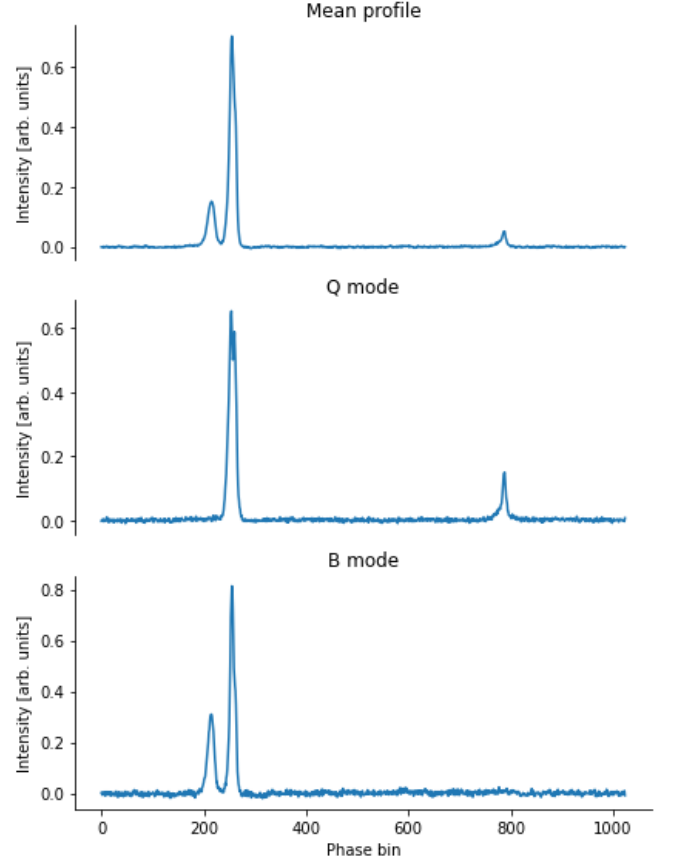


FIG. 3. The mean profile, Q mode and B mode for PSR B1822-09. This figure was created using the normalised raw data from the DFB dataset. The mean profile was created by taking the mean of all profiles and the Q and B modes shown are just one observation where the pulsar showcases one state.

The emission modes of PSR B1822-09 have been extensively studied since they were first reported in 1981<sup>28</sup>. PSR B1822-09 exhibits two main emission modes: a quiet mode (Q mode) and a bursting mode (B mode), sometimes referred to as a bright mode. The former has a dim or non existent PRC but a bright IP and the latter has a bright PRC and weak IP<sup>29, 28, 30</sup>. Petrova et al. (2008) put forward a suggestion that the IP is the result of transverse scattering. Because the IP is seen at a phase of 180°, the IP is generally thought to be the result of the emission and rotation axes being orthogonal so emission from both ends of the pulsar cuts the line of sight of the receiving telescope<sup>31</sup>.

The Q and B mode switching can happen on a scale of under a minute so a single observation may capture a superposition of the two modes. When looking at individual observations for PSR B1822-09, it can be seen that the presence and absence of a PRC and IP are not the only changes in emission profile it undergoes. There is variation in the components present in the MP.

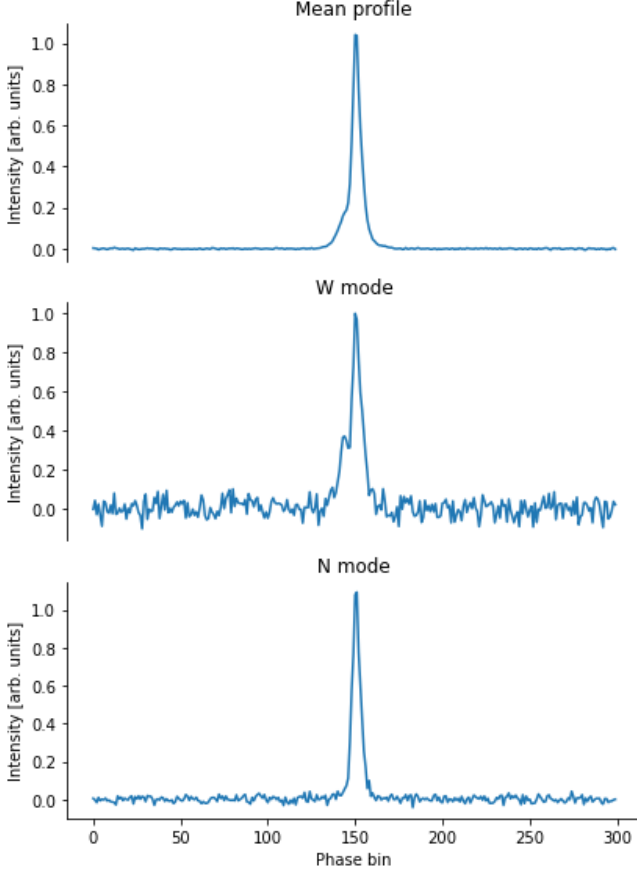


FIG. 4. The mean profile, N mode and W mode for PSR B1828-11. The mean profile was created by taking the mean of all the normalised profiles and the W and N modes shown are just one observation where the pulsar showcases one state.

## 2. PSR B1828-11

It has been seen previously that PSR B1828-11 has two emission modes<sup>621</sup>. The modes will be called a narrower (N) and wider (W) mode. The N mode, shown in figure 4, appears to have only one component and a more intense peak than the W mode. The W mode has a less intense peak and an additional component on the leading edge of the pulse. The W mode shows a higher noise level because the W mode generally has a less intense peak so during normalisation the noise is scaled up. The mean flux of the N mode is around 1.4 that of the W mode<sup>6</sup>.

The physical mechanisms underlying the mode switching seen in PSR B1828-11 are not yet fully explained by any model. There is a need to explain the cyclic and abrupt nature of the changes which there is currently no model for<sup>21</sup>.

## G. PCA

In 1901 PCA was discussed as a way to represent a system of points in space by a line of best fit. The mathematical procedure to find this line of best fit was outlined by minimising the orthogonal distance from each point to the line<sup>32</sup>.

When a dataset has multiple attributes of interest, called features, it is challenging to visualise all the individual features and relationships between them. PCA provides a way of condensing information from different features into components that retain the essential characteristics of the data and can be visualised. This is done by creating principal components (PCs), eigenvectors that encapsulate two dimensional correlation in the data. The more variance along an axis, the more it represents about the data. The first principle component axis (PC1) therefore represents the direction in which the data varies most. More orthogonal principal component axes can be added up to PCn. Identifying PCs can uncover relationships that would not have been initially clear from looking at the data. To study the emission modes of pulsars, the features refer to the intensities at different points along the phase of emission. PC1 should therefore encapsulate the variation between observations with a bright precursor pulse and those with a bright interpulse. If there is one mode we expect the first principal component to have structure and the rest to have very little structure: all the variance in the data can be described by scaling the PC1 by different amounts and adding it to the mean.

First the principal components must be calculated. This is done by finding the line of best fit of the data. The line of best fit is found by maximising distance from the projection of the data points on to the line of best fit to the origin. This is equivalent to minimising distance from points to projection of points onto line, which can be proved using Pythagorean theorem.

This is mathematically equivalent to calculating the covariance matrix of the dataset and finding the eigenvectors,  $v_i$ , and corresponding eigenvalues,  $\lambda_i$  using  $S_i v_i = \lambda_i v_i$ . The eigenvectors correspond to the lines or planes of best fit. The eigenvector with the largest corresponding eigenvalue is PC1 as that has a maximum variance.

The covariance matrix is calculated as follows. It will have as many dimensions as there are features of the data, for a 2D matrix it is:

$$S = \begin{bmatrix} \text{cov}(\mathbf{X}, \mathbf{X}) & \text{cov}(\mathbf{X}, \mathbf{Y}) \\ \text{cov}(\mathbf{Y}, \mathbf{X}) & \text{cov}(\mathbf{Y}, \mathbf{Y}) \end{bmatrix} \quad (7)$$

Each element is calculated using the formula for variance of a sample.

$$\text{cov}(\mathbf{X}, \mathbf{X}) = \frac{1}{n-1} \sum_{i=1}^n (X_i - \bar{X})^2 \quad (8)$$

TABLE II. A summary of the key properties of the different datasets used in this report: the backend used, the epochs over which the data spanned, the number of observations ( $N_{obs}$ ) and the average cadence ( $\langle\Delta t\rangle$ ).

PSR	Backend	Epoch range (MJD)	$N_{obs}$	$\langle\Delta t\rangle/\text{days}$
B1822-09	AFB	45143 - 55335	731	14
B1822-09	DFB	55137 - 60347	882	6
B1828-11	DFB	55202 - 60355	332	16

$$\text{cov}(\mathbf{Y}, \mathbf{Y}) = \frac{1}{n-1} \sum_{i=1}^n (Y_i - \bar{Y})^2 \quad (9)$$

$$\text{cov}(\mathbf{X}, \mathbf{Y}) = \frac{1}{n-1} \sum_{i=1}^n (X_i - \bar{X})(Y_i - \bar{Y}) \quad (10)$$

To perform the PCA we used scikit learn software on python<sup>33</sup>. The code used can be provided on request using the email provided.

### III. METHODS

#### A. Data

Table II gives an overview of the properties of the data used in this experiment which will be discussed subsequently.

##### 1. PSR B1822-09

Pulsar B1822-09 was studied using telescopes at the Jodrell Bank Observatory. The 76 m Lovell Telescope was primarily used with supplementary observations from the 38x25 m Mark II telescope. The data was acquired with one of two pulsar backends: an analogue filterbank (AFB) for the earlier observations and digital filterbank (DFB) from 2009 to present day observations, with a 2 year overlap. DFB data has higher time-resolution<sup>1</sup>.

The AFB data on PSR 1822-09 was collected from Modified Julian Day (MJD) 45143 to MJD 55335 (which corresponds to a period 1982-2010). The data consists of 731 observations, each with the total phase folded onto 400 bins. The average duration of an observation was  $\sim 550$  with a range of 250 s each side of that. One observation would therefore be an integrated pulse of on average 715 individual pulses, using a 1.3 s period from Shaw et al. (2022) (hereafter SSW). Observations were taken at the Jodrell Bank Observatory using the Lovell Telescope at a radio frequency range centred on 1400 MHz (L-band) with a 32 MHz bandwidth. From November 1997 and May 1999 the bandwidth was changed to 96 MHz. Supplementary observations were taken from the Mark II telescope which were centred on 400, 610

and 925 MHz with a bandwidth of 4-8 MHz. Profile shape is frequency dependent so many readings at different frequency bands had to be discarded as we wished to investigate the change in profile over time so frequency change would be a confounding variable.

For the DFB data we used 882 observations collected from MJD 55137 to MJD 60347 (2009-2024 in years). Though some were removed on the basis of their signal to noise ratio obscuring the signal as previously discussed. The average duration was  $\sim 1500$  s meaning the average number of pulses per observation was  $\sim 2000$  which is greater than for the AFB data. The duration of observations for the DFB dataset had a greater range of  $\sim 400$  to 30,000 s. The full phase rotation of the pulsar spanned 1024 bins. The same telescopes were used as for the AFB data but at a central frequency of 1420 MHz and a bandwidth of  $\sim 400$  MHz.

##### 2. PSR B1828-11

The 332 observations used to study PSR B1828-11 were DFB data taken with the Lovell at a frequency of  $\sim 1600$  MHz and bandwidth of 384 MHz, though there were some deviations to the stated frequency and bandwidth. Again, supplementary data was taken with the Mark II telescope. The observations cover MJD 55202 to MJD 60355 (2010 to 2024). The full phase rotation of the pulsar spanned 1024 bins as with PSR B1822-09.

Our data had been pre-aligned as follows. Some observations over the time periods we studied had been removed from the dataset during the alignment process for various reasons: high levels of RFI (radio frequency interference) rendering the signal indistinguishable; the frequency of the observation being different; the number of phase bins being different. The alignment was performed by finding the brightest profile and rotating the array such that the peak was centred on bin 256. Each profile was then shifted so the peak was centred at the same phase using a cross correlation to find how many bins to shift the peak by. Once all the profiles had been rotated to have a common phase they were stacked to provide a high signal to noise (SnR) template profile. The cross correlation was shifted with respect to the high SnR template. The same process was undergone for PSR 1822-09 except the high SnR template was already provided. This introduced a source of uncertainty into the data as if there is more power in a leading component, the cross correlation may be skewed and the peak registered earlier or otherwise if more power is experienced after the peak.

##### 3. Spin-down

$\ddot{\nu}$  is the second derivative of the timing residuals which was found by SSW using a Gaussian process regression (GPR). This time series was smoothed by GPR, whereby in contrast to the sliding boxcar method (discussed in section D) there is

no specified window size. Instead, the model is allowed to learn the window size from the timescale of the periodicity of the data. The processing of the  $\dot{v}$  data had been performed prior to our receiving, for more detail on its calculation see SSW.

## B. Normalisation

Each observation had to be normalised to perform PCA and to meaningfully visualise the data. Three methods of normalisation were attempted and compared in terms of the PCA results they yielded. Firstly peak to peak normalisation was employed by scaling each observation such that the peak value (the highest intensity value out of all the bins for one observation) was equal to 1. This was done by dividing each intensity value by the intensity at the peak. This method had the advantage of being unaffected by noise but introduces high error by using only one value to perform the entire normalisation. If the peak value contains error, this will be disproportionately propagated throughout the normalisation compared to if an average value was calculated and the observations were normalised such that the average was equal to 1 instead of the peak. An average normalisation was attempted but was unsuccessful because the average value of an observation was more determined by the noise level of the observation than the signal. Ideally, the noise would be accurately modelled as Gaussian white noise (GWN) and therefore average to 0 meaning that taking an average of an observation does represent mainly the signal. However, changes in instrumental or atmospheric conditions could mean the noise properties vary over time so the mean of noise changes so it can no longer be modelled as GWN. This is likely where the issue arises in using average normalisation. An unsuccessful normalisation manifested graphically as the stacked intensity heat map showing variation between observations rather than between on and off pulse regions.

In an attempt to reduce the high error introduced by using solely the peak value for normalisation, Gaussian fitting normalisation was performed. The initial step was to create an average pulse profile for the main pulse which was done by calculating the average intensity across all observations for each bin. Next, a Gaussian was fit to the main pulse using the Scipy Curve Fit function. Performing a Gaussian fit relies on adjusting the mean, standard deviation and amplitude however to make the code run faster we only fit the amplitude parameter for each observation. This was possible because the data we were working with had already been aligned so the mean and standard deviation were constant across observations. Finally, each observation was scaled by a factor  $\frac{A_{av}}{A_{obs}}$  where  $A_{av}$  is the amplitude of the average profile and  $A_{obs}$  is the amplitude of the observation being scaled. It was predicted that this method of normalisation would produce better results, because it relies on the whole profile of the pulse not just the peak value. We found that there was very little difference compared to normalisation using just the peak.

## C. Selection of observations

Some observations exhibited noise and interference rather than signal resembling a pulse. If left in the dataset, these observations affect the eigenvalues obtained from PCA, obscuring the useful information and patterns in the data. For example, in the DFB dataset, observations in the 400 to 500 range often show no pulse but periodic noise variation. These observations coincide with the switch to the Mark II telescope which would be expected as a smaller diameter dish means reduced sensitivity to faint radio signals. Identifying which observations to remove was challenging as it relied on subjective judgement. We aimed to keep as many observations as possible to maintain a robust dataset to base conclusions off but also filter out observations that were interfering with the analysis as they were the product of RFI not the pulsar. The most effective way found, that relied least on subjectivity, was determining an SnR for each observation and discarding observations below a certain threshold. The threshold was determined by adjustment and inspection of the shape parameter, maximising the number of credible pulses left in the dataset. The SnR ratio was calculated using the maximum intensity value as the signal and the standard deviation of a selected number of bins in the off pulse region as the noise.

## D. Smoothing

Smoothing is a method of data processing employed to reduce noise on a time-series data enabling emergent patterns to be more clearly visualised. We used smoothing on the shape parameters to determine if there were key patterns obscured by noise. A ‘sliding boxcar’ method was used whereby a step size and window size was selected then the average of all the points in that window was taken, the window was moved along by the step size and the average of that window was taken, until a new array was created with less points that represented an averaged version of the original shape parameter, less sensitive to noise. Window size can be manipulated to reveal different aspects of the data. A smaller window size will allow visualisation of events happening on a smaller timescale and a larger one will remove variation on a smaller timescale enabling the longer timescale events to be seen clearly.

## E. Heat maps

The observations were not taken at evenly spaced intervals and therefore to create a colour-map of the intensities of the pulses linear to the times of observation some observations are ‘smeared’ across the graph to represent the fact there was no observation between that time and the next. This was done by creating a list of days of even spacing, starting the day of observation 1 and ending at the day of the final observation with each entry increasing by 1 day. For each day of this evenly spaced list of days, the observation with the nearest day of recording was found and appended to a new matrix such that



each column of the new matrix represented the intensity of the pulse at equally spaced increments of time.

#### F. Correlation Coefficient

To quantify the correlation between the shape parameter and the  $\dot{v}$  time-series a Spearman's rank correlation coefficient ( $\rho$ ) was calculated using the Scipy stats module<sup>34</sup>. A Spearman's rank is calculated by ranking the data from highest to lowest and comparing point by point the data with the same rank; it tests for a monotonic relationship.  $\rho$  values of -1 or +1 imply a perfectly monotonic relationship while if  $\rho = 0$  this implies no correlation. Spearman's rank was chosen over methods that find linear correlation, like Pearson's rank, as correlation may not be linear. Furthermore, Spearman's rho makes no assumptions about the data distribution which was necessary as the points being compared from the two time series were not necessarily at equally spaced intervals. The shape parameter time series was resampled to match the length of the  $\dot{v}$  time series to perform the correlation. This was done by interpolating the un-smoothed SP to find the SP value at dates corresponding to the observation date of each entry in  $\dot{v}$ . The cubic spline method of interpolation was used for its capability in dealing with non linear relationships like that present in the SP time series. The interpolation was done implementing the same Scipy stats module<sup>35</sup>.

The error quoted on the  $\rho$  values was calculated using bootstrapping. This is a technique whereby the data is shuffled a number of times (N) to produce a new dataset.  $\rho$  is re-calculated for each new dataset. A distribution is then produced of the new  $\rho$  values which should be a Gaussian centred at 0 as the correlation between a dataset and a randomly shuffled dataset should average to 0 over a large N. The uncertainty is then the standard deviation of this distribution.

### IV. RESULTS AND DISCUSSION

#### A. Recreating the stacked intensities with PCA method

By applying PCA to the data we obtained an eigenvector, eigenvalues and explained variance for as many principal components as was specified in the PCA function. The eigenvectors are of the same length as the number of bins in the observation used and capture the variation in intensity of the bins across the dataset, they are referred to as the principal components (PCs). For a visual representation of a PC see the right panels of figure 6. The PC is accompanied by eigenvalues (as many eigenvalues as observations) which denote 'how much' of that PC is in the observation. The explained variance is how much of the variation in the dataset is explained by that component. This may be clarified by an equation: the reconstructed profile for observation  $i$  which has  $j$  bins is:

$$profile_i(j) = \overline{PC} + \sum_i C_i PC_i(j) \quad (11)$$

where  $\overline{PC}$  is the mean of the dataset and this is added to the PC multiplied by the eigenvalue  $i$  which is specific to that observation. This involves multiplying all  $j$  values in the PC array by 1 eigenvalue for that principal component, essentially using the eigenvalue as scaling factor. This is the case where the number of principal components,  $n$ , used is 1 but the procedure is the same when  $n > 1$ . Each PC is multiplied by its corresponding eigenvalues for each observation creating  $n$  arrays length  $j$ . The arrays are then summed element-wise to form one array length  $j$ . This is then added to  $\overline{PC}$  to create the reconstructed profile.

It was found that the  $n$  used in PCA had little to no effect on the shape parameter. So, whilst for other studies the number of PCA components used would depend on how many were needed for the explained variance to exceed a certain threshold, the  $n$  used here did not affect the final results. We instead changed the number of components to inspect up to what number the PCs contained structure and at what point they modelled noise.

The PCA reconstruction performed using equation 11 is shown in figure 5 (lower panel) in comparison to the original dataset (top panel). The number of bins shown is reduced on the figure to make the areas of interest, the pulses, clearer. However this was also the number of bins used to train the PCA to allow it to train on the on pulse regions so it would model the variation here rather than in the noise. It was found that like  $n$ , the bins used to train the data on had little to no effect on the shape parameter, presumably because the largest variation was in the on pulse regions so the PCA would capture variability here rather than in the noise anyway. The PCA reconstruction plot is a representation of the stacked intensity plot where each observation is represented by a reconstructed version of itself with the mean and then an eigenvalue representing how much it varies from that mean value. This enables analysis of the pulse profile over time because it extracts a parameter determining how much each observation varies from the mean. The fact that the PCA reconstruction clearly mirrors the changes in emission in the raw data demonstrates that the PCA is working in the way intended to identify key variation across observations.

#### B. PSR B1828-11 DFB

The most striking result from performing PCA on the data for PSR B1928-11 is that there is structure only in the first PC. This can be seen in the right column of figure 6 as PC2, 3 and 4 show noisy signals that when shown over a larger phase range look like GWN. This figure shows only a small section of the phase capturing the pulse and a little of the noise but when looking at the full phase cycle of the pulsar it is clear that higher order PCs than PC1 mainly model noise. This is reinforced by the variation maps on the left column of figure 6: instead of showing variations in the on pulse region, the higher order components model variation across the on and



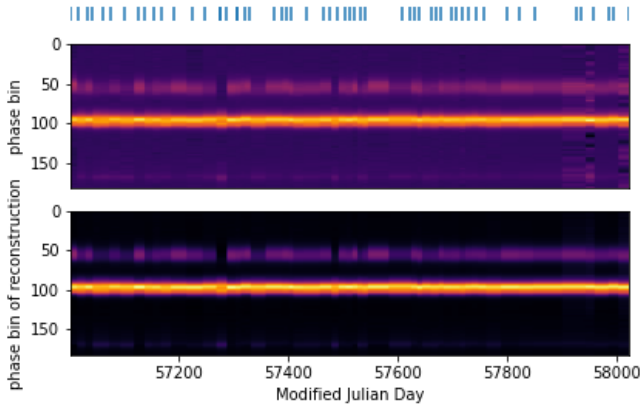


FIG. 5. A heat map of the intensities of the original dataset is shown on the first panel and the second shows how the PCA reproduces this. This shows only a 1000 day window so the modes in individual observations is more distinguishable. The observations have been evenly spaced according to the method outlined above. The IP is seen around bin 50, the MP around bin 100 and the PRC around bin 120.

off pulse bins and therefore are likely to be modelling noise instead of changes to emission mode. All the profile variation can be captured by one principal component suggesting the simplest model to describe the emission would be a two state system. This is because all the variation in the data can be projected onto one dimension of variation so each observation of the dataset can be adequately described by the mean plus PCA component, the amounts of which are determined by the SP. If the shape parameter displays a bimodal distribution, the system can then be said to be a two state system.

The shape parameter, shown in figure 8, shows which state the system is in and how it evolves over time. The shape parameter exhibits a double peak structure (a larger peak followed by a smaller peak) which is also exhibited by PSR B0919+06<sup>36</sup>. It is tempting to assume this indicates a three state system, with emission states centred at -0.4, an intermediary state, and +0.4. However inspection of the unsmoothed shape parameter, shown in figure 7, reveals that the pulsar is likely in a two state system but the act of smoothing the data and the fact that observations are integrated pulses that can contain a mixture of two states gives the smaller peak that could be interpreted as a third state. Where the smaller peaks can be seen in the smoothed shape parameter, the unsmoothed shape parameter shows oscillations on a scale as small as days between the higher and lower states that average to an intermediary state after smoothing over the 100 day window. Smaller peaks can be seen on the shape parameter but these could be due to switches in state that occur during one observation giving rise to an integrated profile that is a mix of both states. It is therefore likely that the double peak structure of the shape parameter is the result of state switching on a smaller timescale than that of the observation and due to smoothing rather than the fact that the pulsar is in a 3 emission state system.

The bottom two panels of figure 9 show that the  $\dot{\nu}$  and the shape parameter are correlated, which is in accordance with what was found in LHK and SSW. We found a correlation coefficient of  $\rho = 0.66 \pm 0.06$ . The correlation coefficients are summarised in table III. From figure 9 it is clear that the states where the power is more spread about the MP and there is less power in the central component of the MP (the W mode) correlate to a slower  $\dot{\nu}$  rate. When the power is concentrated in the central component (the N mode) there is generally a faster  $\dot{\nu}$  rate. Radio emissions are a flux of particles out of the magnetosphere which induce torque on the pulsar slowing it down<sup>7</sup>. It has been shown that there is an increased flux in the N mode causing increased torque and therefore a higher  $\dot{\nu}$ <sup>6</sup> so the result found here that N mode correlates to a faster  $\dot{\nu}$  is inkeeping with current predictions.

### C. PSR B1822-09 AFB

The principal components analysis and corresponding variation maps are shown on figure 10. On the right hand panel of the top row, PC1 can be seen to have a distinct structure where the PRC, MP and IP can be distinguished at around phase bins 20, 35 and 58 respectively. The PRC and IP are anti-correlated which is to be expected as when there is more power in the PRC there is less in the IP and vice versa. PC1 captures the variation relating to the Q and B emission modes, suggesting this is the largest source of variation in the data which was expected from LHK and SSW. It can also be seen from PC1 that when the IP is brighter the MP is wider with a less intense peak but in the B mode the MP is narrower with a more intense peak. This is most evident looking at the PC1 difference map on the top left panel of figure 10.

PC2 also shows structure: it represents variation in the components present in the MP. There is a leading component which comes earlier in the rotational phase and a trailing component of the MP which are anti-correlated, so when one is present the other is suppressed. The IP is correlated with the trailing component (so anti-correlated with the leading component) and the precursor is correlated with the leading component (and anti-correlated with the trailing component). The variation of components in the main pulse must be occurring on a different timescale to the Q and B mode switching otherwise both would have been picked up on by the same principal component. We therefore show that the emission of PSR B1822-09 cannot be adequately described by a two state system.

The difference maps, shown in the left column of figure 10, show the contribution of the principal component in each observation so the variation captured by the principal component can be seen over time. Lighter regions of the difference map represent higher intensity and darker regions lower intensity. The variation map for PC1 shows the anti-correlation between the PRC and IP and also the width of the MP associated with both the Q and B modes. It shows how

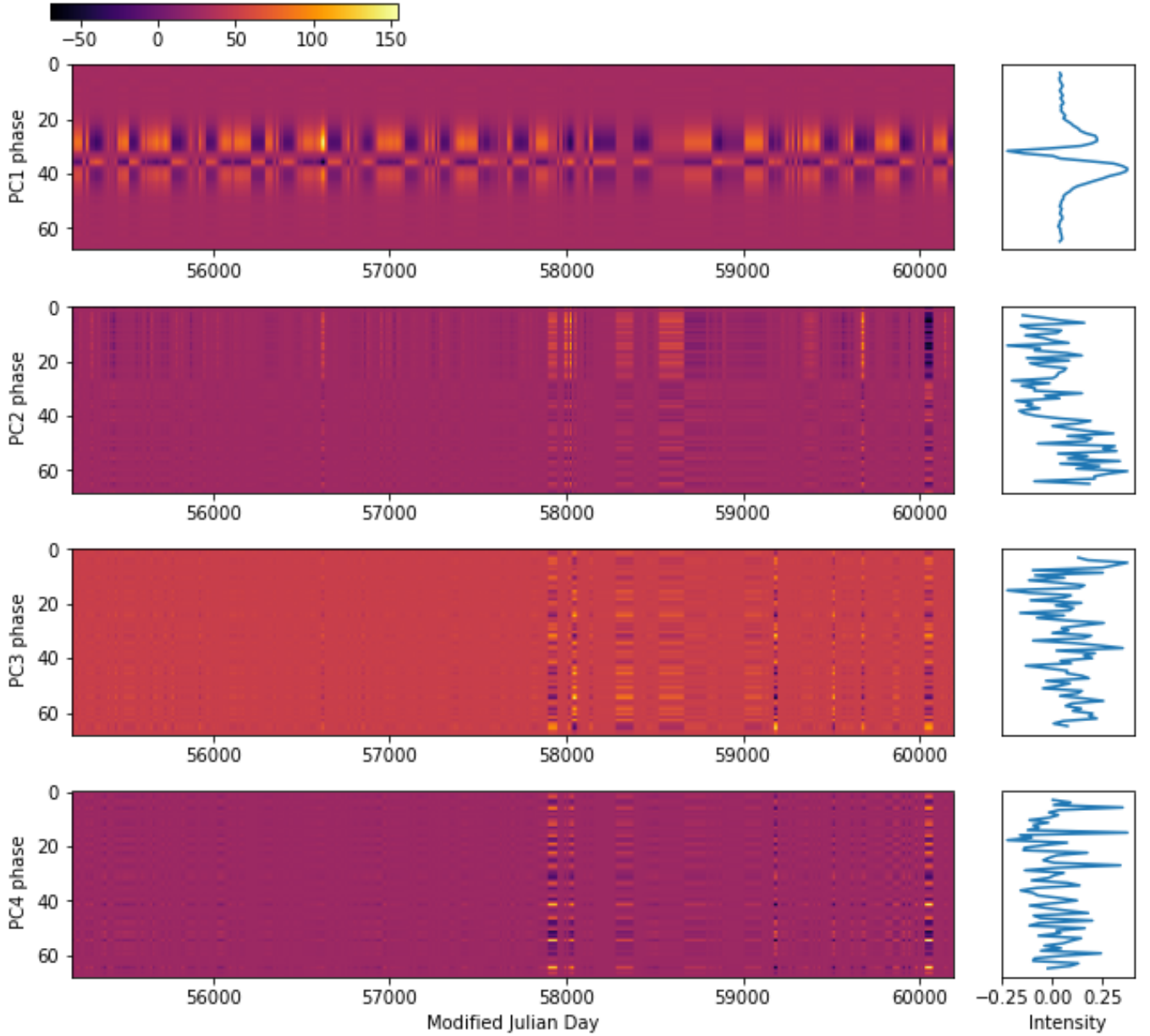


FIG. 6. The left column is the variation map showing what that PC is representing over time. The right column shows the principal component with intensity on the x-axis and the same phase as the variation map. The scale of the PC intensities is not shown for all components as it is the relative contributions of components that is of interest not the scale.

these evolve over time: the pulsar oscillates between the Q and B states, sometimes quicker and sometimes slower, which can also be seen in the original pulse stack. The variation map for PC2 is mostly concerned with the components comprising the MP as expected from the shape of PC2. The variation maps show that the mode switches captured by PC1 and PC2 occur at different timescales. This could perhaps suggest they have different origins in terms of their emission mechanisms.

PC3 and PC4 arguably also show structure and the timescales of the variation they capture can be seen in the variation maps. The differences in intensities captured by the

variation maps decrease for each PC, demonstrating how less variance is captured by higher order PCs.

The fact that there is structure in higher order principal components suggests more than a simple two state system which leads to the question of which shape parameter to use in comparison to the  $\dot{\nu}$  rate. It could be suggested that the shape parameter associated with PC1 captures most of the variation in the data and therefore the mode switches described by PC1 would have the most significant impact on the  $\dot{\nu}$  and thus the highest correlation. However, though PC1 identifies the dimension of highest variation in the data,

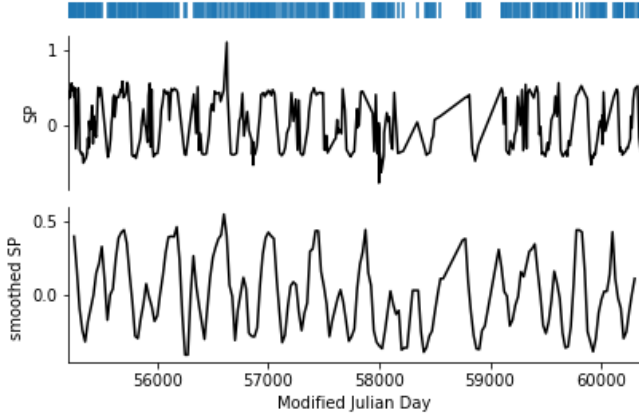


FIG. 7. The blue lines above the axes show the cadence: each line marks the epoch of an observation. The top plot shows the shape parameter un-smoothed and the bottom plot is the smoothed version with a window size of 100 days.

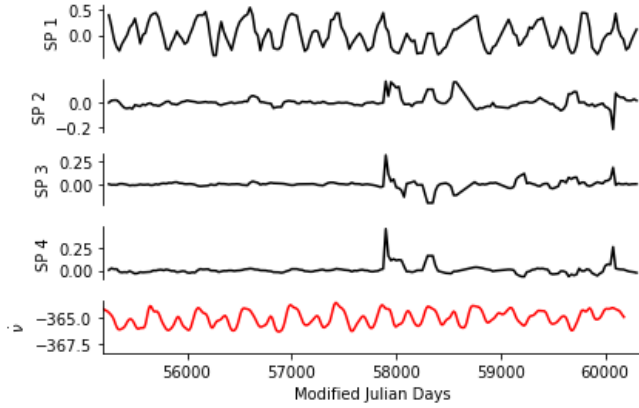


FIG. 8. The shape parameters for PSR B1828-11 are shown in black, aligned with the  $\dot{\nu}$  in red for comparison. All shape parameters have been smoothed with a window size of 100.

the data may not capture the most variation in the pulsar emission. The pulse profiles we receive are only a small cut through the whole beam so perhaps the Q and B mode changes are insignificant compared to changes happening elsewhere in the beam which could be more correlated to  $\dot{\nu}$ . It could also be that the variation picked up on by PC2, for example, is part of a more significant phenomena to the whole pulsar beam but only a small part is picked up due to our line of sight so it is worth investigating whether any higher order shape parameters correlate to the  $\dot{\nu}$ . A small change in the profile may represent a large change in the pulsar so it must be considered that the lack of correlation seen may not be a lack of correlation between emission mode and  $\dot{\nu}$  but more that the profiles we see do not capture the large changes in emission.

The shape parameters for higher order PCs were therefore investigated and are shown on figure 11. The shape parameters corresponding to the different PCs are shown above

each other so the timescale of the different mode switches can be visualised. The correlation coefficients were found to be  $0.13 \pm 0.04$ ,  $-0.04 \pm 0.04$ ,  $-0.16 \pm 0.04$  and  $-0.04 \pm 0.04$  for SP1, SP2, SP3 and SP4 respectively. All variation in emission captured by PCA is therefore almost uncorrelated with  $\dot{\nu}$ . On inspection of SP 1 on figure 11 on figure 11 it can be seen that some of the peaks do correlate with peaks in spin-down rate but there are too many peaks in SP1 to claim statistical significance to these alignments. This contrasts to the conclusion from the LHK that  $\dot{\nu}$  and shape parameter were highly correlated over this time period. Perhaps the discrepancy lies in the selection of observations. Whilst the second spike in  $\dot{\nu}$  is mirrored by a change in SP1, it is unclear the relation between the third spike and SP1 due to lack of cadence in this region. The third spike in  $\dot{\nu}$  occurs at around MJD 52000 and many of the observations were removed from this region due to RFI contamination<sup>1</sup> which could obscure correlation between  $\dot{\nu}$  and SP1. It is unlikely however that observations in this region would lead to a rejection of the hypothesis that  $\dot{\nu}$  is not highly correlated with any of the shape parameters as there are many spikes in SP that are not accompanied by any change in  $\dot{\nu}$ . These findings support what was found in SSW: there is no strong correlation between  $\dot{\nu}$  and emission state.

The lack of correlation of SP1 and  $\dot{\nu}$  would suggest that the Q and B mode switching does not have a profound effect on the torque exerted on the pulsar. Perhaps the Q and B mode switching does not make up a significant enough amount of the overall changes in the magnetosphere and therefore emission profile to correlate to the  $\dot{\nu}$ . However it may still be the case that if all the emission changes were combined in some way all the changes in the magnetosphere would be modelled and thus there would be a correlation with  $\dot{\nu}$ . Adding the SPs of all PCs that show structure would not suffice as the direction of the peaks of the shape parameters are arbitrary due to the nature of eigenvalues extracted by PCA. This could be attempted as an extension of the project however it may be futile as perhaps the changes in emission that affect  $\dot{\nu}$  are occurring at other frequencies than the radio frequency studied here. Given that LHK found a correlation at this frequency, perhaps PCA does not provide a suitable algorithm for extracting the shape parameter such that it correlates

#### D. PSR B1822-09 DFB

PC1 captures the variation between the Q and B modes demonstrating this is the source of the most variation in the dataset, as expected. It can, however, be seen from figure 12 that the variation in this mode is not strongly correlated to the  $\dot{\nu}$  with a correlation coefficient calculated to be  $\rho = -0.05 \pm 0.04$  which is close to 0, supporting the idea of little to no correlation. This result was more unexpected as the mode switching from the dominant mode (Q and B) was predicted to be correlated to the  $\dot{\nu}$ <sup>27</sup>.

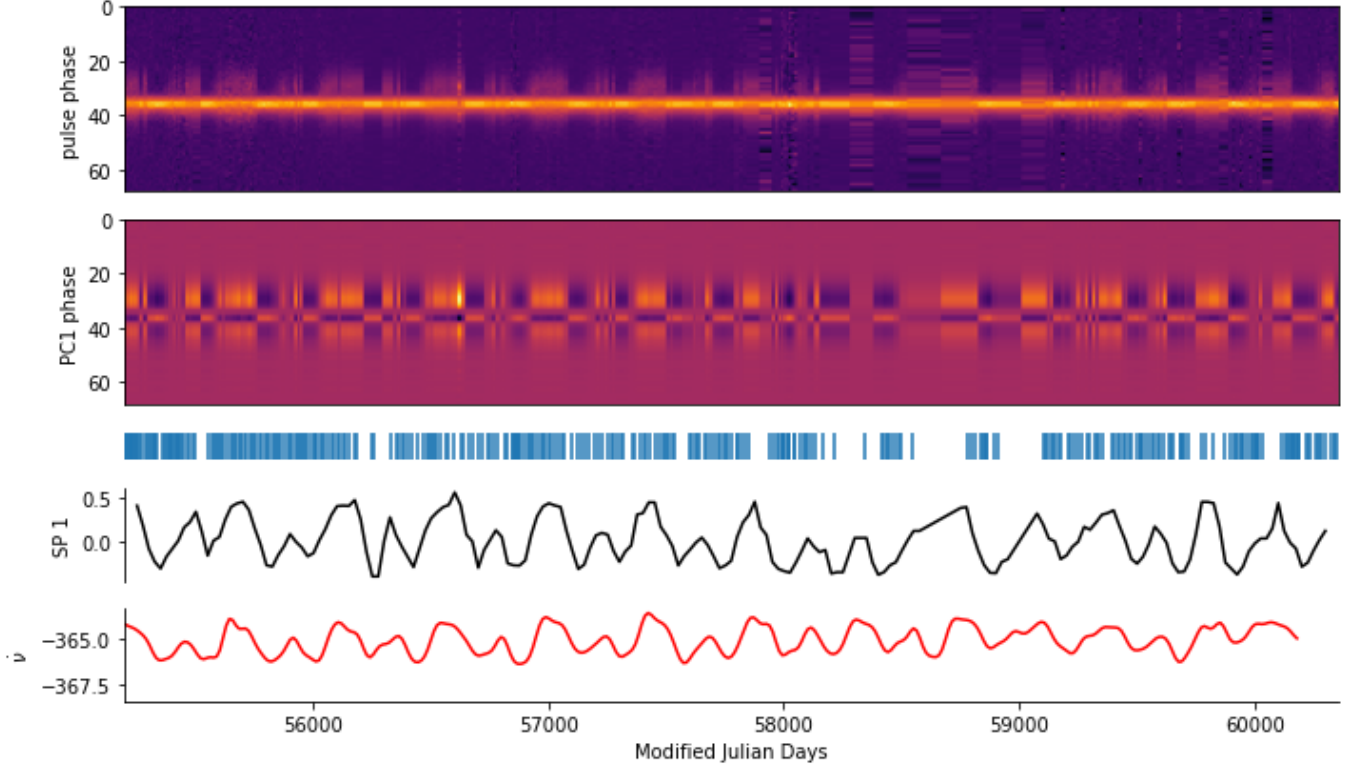


FIG. 9. SP1 for PSR B1828-11. The top plot is a heat map of original data, followed by a variation map for PC1, the cadence is then shown. Below the cadence SP1 is plotted with  $\dot{v}$  beneath it. All subplots have the same axis so events can be compared across the plots.

PC2 captures a noisier signal, picking up the PRC, MP and IP but this time a correlation between the PRC and IP. The variation map shows that the variation captured by PC2 is a change in profile around MJD 58000. There is more power in the PRC and IP before MJD 58000 and less power after this date. The overall effect of the change is more concentrated power in one component of the MP after MJD 58000. MJD 58000 corresponds to the date of the first  $\dot{v}$  peak in the DFB dataset so perhaps there was a change in the magnetosphere giving rise to a brighter component in the MP which also caused more  $\dot{v}$  events as the  $\dot{v}$  time series shows slightly higher small peaks and the three large peaks after MJD 58000. The average  $\dot{v}$  after MJD 58000 is slower which corresponds to an average trend of in emission state to be more concentrated in one component of the MP. This could be a reason that the correlation coefficient  $\rho = 0.26 \pm 0.04$  is higher for PC2 than the other components: it reflects a general correlation rather than correlation between specific  $\dot{v}$  events and shape parameter peaks.

PC3 seems to capture a similar phenomena to PC2 and PC3 for the AFB data: the power in different components making up the main pulse. There is an extra level of detail in DFB PC3: a correlation between the intensity of the leading component of the MP and a sub peak in the trailing component of the MP. This detail could be the result of the higher resolution of the DFB backend or the frequency

TABLE III. The  $\rho$  between the shape parameter and  $\dot{v}$  shown for the first 4 shape parameters for the different pulsars and pulsar backends.

Shape parameter	$\rho$		
	B1828-11 DFB	B1822-09 AFB	B1822-09 DFB
SP1	$0.66 \pm 0.06$	$0.13 \pm 0.04$	$-0.05 \pm 0.04$
SP2	$0.00 \pm 0.06$	$-0.04 \pm 0.04$	$0.26 \pm 0.04$
SP3	$-0.11 \pm 0.06$	$-0.16 \pm 0.04$	$0.14 \pm 0.04$
SP4	$0.28 \pm 0.06$	$-0.04 \pm 0.04$	$0.10 \pm 0.04$

difference in datasets giving rise to difference in pulse profile. Observations using the DFB backend at 1400 MHz would have to be taken to identify which is the case.

Whilst PC4 begins to model more noise, some structure is still visible so it is still measuring some changes to profile over the dataset. There is structure up to around the eighth PC of the DFB dataset whereas the AFB begins modelling noise around the 4th component. It is still difficult to attribute this difference to either frequency or resolution without more DFB data at 1400 MHz. Structure up until the eighth component is a stark contrast to PSR B1828-11 showing that if PSR B1822-09 was in a two state system the higher order PCs would model just noise. The fact that there is structure up to the eighth component shows the pulsar is exhibiting complex emission changes that cannot be modelled by a simple system.



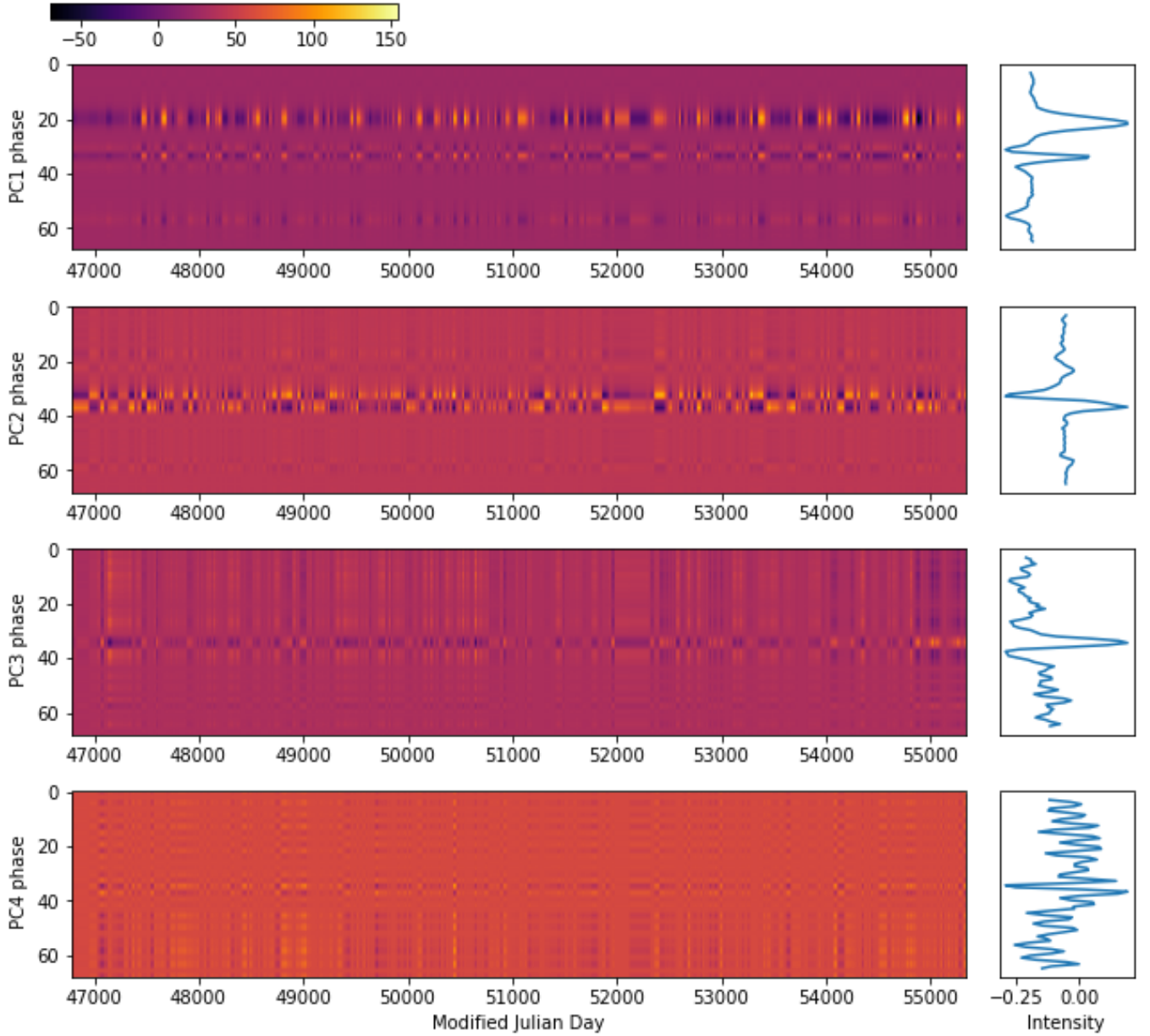


FIG. 10. Variation maps are shown in the left column and their corresponding PCs in the right column for PSR B1822-09 AFB. The phase of the variation maps and PCs correspond.

## V. CONCLUSION

We have shown that PCA can be used to extract the emission modes from pulsars and quantify their time evolution. We found similar results to those obtained by SSW by using PCA instead of GPR to characterise the emission modes and extract shape parameters for PSR B1828-11 and PSR B1822-09. For PSR B1828-11 we found a correlation of  $0.66 \pm 0.06$  linking the W mode to a slower  $\dot{\nu}$  and the N mode to a faster  $\dot{\nu}$ . PSR B1822-09 did not exhibit a simple two state system and the  $\dot{\nu}$  was found to be largely uncorrelated with the shape parameters, supporting findings from SSW. Perhaps if the contribu-

tions from all different emission modes were combined (by considering all the SPs), a correlation would be found. PCA could be used to characterise emission profiles from other frequencies for PSR B1822-09 to determine whether there is a link between emission state and  $\dot{\nu}$  elsewhere in the spectrum. It would be an interesting extension to study the smaller timescale events for example whether a switch in the Q and B mode was followed by a change in which components are present in the main pulse for PSR B1822-09. PCA would provide a useful framework to do so as changes in emission state can be easily quantified over time. The method used is highly generalisable to other pulsars as the algorithm selects the key behaviours to extract, relying on very little implicit informa-

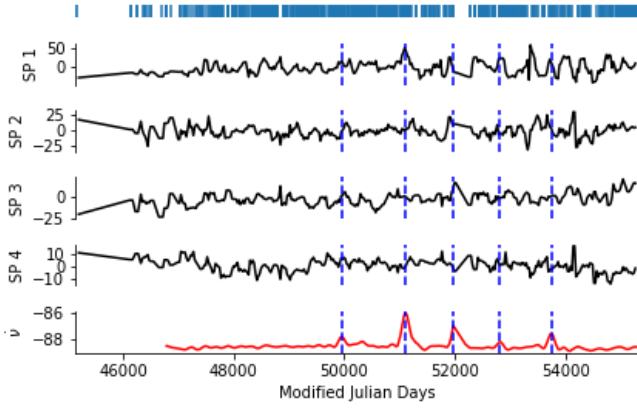


FIG. 11. First 4 SPs for PSR B1822-09 AFB shown in black with  $\dot{v}$  to compare. The SPs have been smoothed with a window size of 100. Blue lines show the peaks of the spin-down events.

tion. Application to wider populations of pulsars would not, therefore, be too time consuming and may reveal aspects of their behaviour that other methods have not.

- <sup>1</sup>B Shaw, B W Stappers, P Weltevrede, P R Brook, A Karastergiou, C A Jordan, M J Keith, M Kramer, and A G Lyne. Long-term rotational and emission variability of 17 radio pulsars. *Monthly Notices of the Royal Astronomical Society*, 513(4).
- <sup>2</sup>Andrew Lyne, George Hobbs, Michael Kramer, Ingrid Stairs, and Ben Stappers. Switched magnetospheric regulation of pulsar spin-down. *Science*, 329(5990):408–412, July 2010.
- <sup>3</sup>A. Hewish, S. J. Bell, J. D. H. Pilkington, P. F. Scott, and R. A. Collins. Observation of a rapidly pulsating radio source. *Nature*, 217(5130):709–713, February 1968.
- <sup>4</sup>Andrew Lyne and Francis Graham-Smith. *1 The discovery of pulsars*, page 1–15. Cambridge Astrophysics. Cambridge University Press, 2012.
- <sup>5</sup>Andrew Lyne and Francis Graham-Smith. *2 Neutron stars*, page 16–26. Cambridge Astrophysics. Cambridge University Press, 2012.
- <sup>6</sup>P. R. Brook, A. Karastergiou, S. Johnston, M. Kerr, R. M. Shannon, and S. J. Roberts. Emission-rotation correlation in pulsars: new discoveries with optimal techniques. *Monthly Notices of the Royal Astronomical Society*, 456(2):1374–1393, 12 2015.
- <sup>7</sup>M Kramer, AG Lyne, J O’Brien, Christine Jordan, and D Lorimer. A periodically active pulsar giving insight into magnetospheric physics. *Science (New York, N.Y.)*, 312:549–51, 05 2006.
- <sup>8</sup>A. Wolszczan and D. A. Frail. A planetary system around the millisecond pulsar PSR1257 + 12. *Nature (London)*, 355(6356):145–147, January 1992.
- <sup>9</sup>DC Backer and RW Hellings. Pulsar timing and general relativity. *Annual review of astronomy and astrophysics*, 24(1):537–575, 1986.
- <sup>10</sup>Ingrid H. Stairs. Testing General Relativity with Pulsar Timing. *Living Reviews in Relativity*, 6(1):5, September 2003.
- <sup>11</sup>G. B. Hobbs, R. T. Edwards, and R. N. Manchester. tempo2, a new pulsar-timing package – I. An overview. *Monthly Notices of the Royal Astronomical Society*, 369(2):655–672, 05 2006.

- <sup>12</sup>Andrew Lyne and Francis Graham-Smith. *5 Pulsar timing*, page 61–75. Cambridge Astrophysics. Cambridge University Press, 2012.
- <sup>13</sup>Jones. Pulsar state switching, timing noise and free precession. *Monthly Notices of the Royal Astronomical Society*, 420(3):2325–2338, 02 2012.
- <sup>14</sup>K. Liu, Y. L. Yue, and R. X. Xu. Psr b1828–11: a precession pulsar torqued by a quark planet? *Monthly Notices of the Royal Astronomical Society: Letters*, 381(1):L1–L5, October 2007.
- <sup>15</sup>*Neutron Star Models: Masses and Radii*, chapter 9, pages 241–266. John Wiley Sons, Ltd, 1983.
- <sup>16</sup>*Pulsars*, chapter 10, pages 267–305. John Wiley Sons, Ltd, 1983.
- <sup>17</sup>Gordon Baym, Christopher Pethick, and David Pines. Superfluidity in neutron stars. *Nature*, 224:673–674, 1969.
- <sup>18</sup>J. Urama. Glitch monitoring in psrs b1046-58 and b1737-30. *Monthly Notices of The Royal Astronomical Society - MON NOTIC ROY ASTRON SOC*, 330:58–62, 02 2002.
- <sup>19</sup>Kochukhov, O., Hackman, T., Lehtinen, J. J., and Wehrhahn, A. Hidden magnetic fields of young suns. *AA*, 635:A142, 2020.
- <sup>20</sup>M. Breed, C. Venter, A. K. Harding, and T. J. Johnson. The effect of an offset-dipole magnetic field on the vela pulsar’s gamma-ray light curves, 2015.
- <sup>21</sup>I H Stairs, A G Lyne, M Kramer, B W Stappers, J van Leeuwen, A Tung, R N Manchester, G B Hobbs, D R Lorimer, and A Melatos. Mode switching and oscillations in psr b1828–11. *Monthly Notices of the Royal Astronomical Society*, 485(3):3230–3240, March 2019.
- <sup>22</sup>Peter Goldreich and William H. Julian. Pulsar Electrodynamics. *Astrophys. J.*, 157:869, August 1969.
- <sup>23</sup>M. A. Ruderman and P. G. Sutherland. Theory of pulsars: polar gaps, sparks, and coherent microwave radiation. *Astrophys. J.*, 196:51–72, February 1975.
- <sup>24</sup>Andrew Lyne and Francis Graham-Smith. *19 The emission mechanisms*, page 267–278. Cambridge Astrophysics. Cambridge University Press, 2012.
- <sup>25</sup>Joanna M. Rankin. Toward an Empirical Theory of Pulsar Emission. VI. The Geometry of the Conal Emission Region. *Astrophys. J.*, 405:285, March 1993.
- <sup>26</sup>D. C. BACKER. Pulsar nulling phenomena. *Nature*, 228(5266):42–43, 10 1970.
- <sup>27</sup>Andrew Lyne. Timing noise and the long-term stability of pulsar profiles. *Proceedings of the International Astronomical Union*, 291:183–188, March 2013.
- <sup>28</sup>L. A. Fowler, D. Morris, and G. A. E. Wright. Unusual properties of the pulsar PSR 1822-09. , 93:54–61, January 1981.
- <sup>29</sup>J. A. Gil, A. Jessner, J. Kijak, M. Kramer, V. Malofeev, I. Malov, J. H. Seiradakis, W. Sieber, and R. Wielebinski. Multifrequency study of PSR 1822-09. , 282:45–53, February 1994.
- <sup>30</sup>L. A. Fowler and G. A. E. Wright. Pulse-interpulse interaction in pulsar PSR 1822-09. , 109:279–281, May 1982.
- <sup>31</sup>S. A. Petrova. Physics of interpulse emission in radio pulsars. *The Astrophysical Journal*, 673(1):400–410, January 2008.
- <sup>32</sup>K. Pearson. On lines and planes of closest fit to systems of points in space. *Philosophical Magazine*, 2:559–572, 1901.
- <sup>33</sup>The SciPy community. *sklearn.decomposition.PCA*, 2024.
- <sup>34</sup>The SciPy community. *scipy.stats.spearmanr*, 2024.
- <sup>35</sup>The SciPy community. *scipy.interpolate.CubicSpline*, 2024.
- <sup>36</sup>B. B. P. Perera, B. W. Stappers, P. Weltevrede, A. G. Lyne, and C. G. Bassa. Understanding the spin-down rate changes of psr b0919+06. *Monthly Notices of the Royal Astronomical Society*, 446(2):1380–1388, November 2014.
- <sup>37</sup>Edward Witten. Cosmic separation of phases. *Phys. Rev. D*, 30:272–285, Jul 1984.

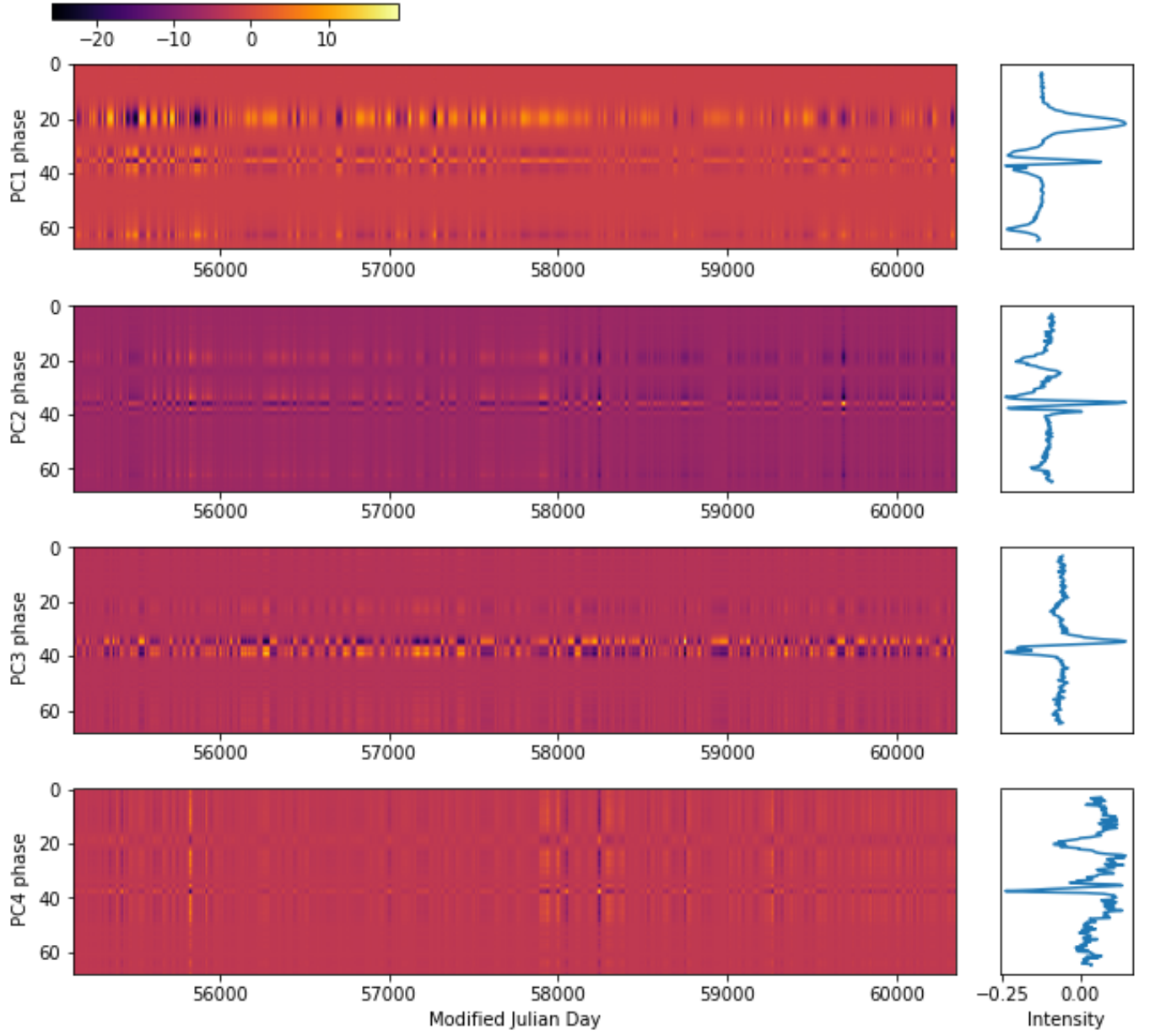


FIG. 12. Variation maps are shown in the left column and their corresponding PCs in the right column for PSR B1822-09 DFB. The phase of the variation maps and PCs correspond.



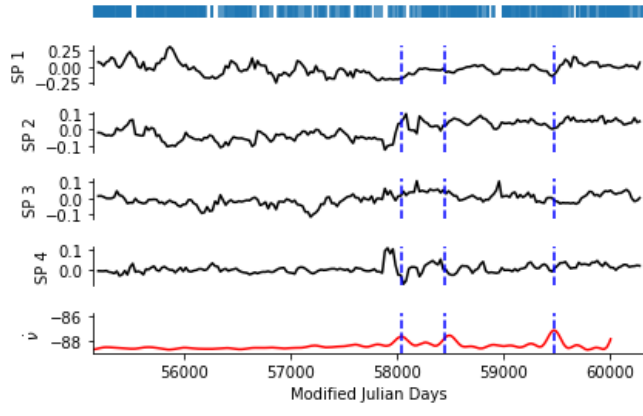


FIG. 13. First 4 SPs for PSR B1822-09 DFB shown in black with  $\dot{\nu}$  to compare. The SPs have been smoothed with a window size of 100.